Mechanisms and functions of respiration-driven gamma oscillations in the piriform cortex

Joaquín González[1*], Pablo Torterolo[1] & Adriano BL Tort[2*]

1 – Departamento de Fisiología, Facultad de Medicina, Universidad de la República, Montevideo, 11200, Uruguay

2 – Brain Institute, Federal University of Rio Grande do Norte, Natal, RN 59056, Brazil

* Correspondence: joaqgonzar@gmail.com or tort@neuro.ufrn.br

Summary

Gamma oscillations are believed to underlie cognitive processes by shaping the formation of transient neuronal partnerships on a millisecond scale. These oscillations are coupled to the phase of breathing cycles in several brain areas, possibly reflecting local computations driven by sensory inputs sampled at each breath. Here, we investigated the mechanisms and functions of gamma oscillations in the piriform (olfactory) cortex of awake mice to understand their dependence on breathing and how they relate to local spiking activity. Mechanistically, we find that respiration drives gamma oscillations in the piriform cortex, which are inhibitory and result from recurrent connections between local excitatory and inhibitory neuronal populations. Moreover, respiration-driven inhibitory gamma oscillations are triggered by the activation of mitral/tufted cells in the olfactory bulb and are abolished during anesthesia. Functionally, we demonstrate that they locally segregate neuronal assemblies through a winner-take-all computation leading to sparse odor coding during each breathing cycle. Our results shed new light on the mechanisms of gamma oscillations, bridging computation, cognition and physiology.

Keywords: neural oscillations, breathing, neuronal assemblies, sparse coding, optogenetics, winner-take-all.

Introduction

Since their discovery by Adrian in 1942, gamma oscillations have been one of the most studied brain rhythms (Bragin et al., 1995; Buzsáki and Wang, 2012; Csicsvari et al., 2003; Fries et al., 2007; Gray et al., 1989; Sirota et al., 2008; Womelsdorf et al., 2006). Gamma is believed to be critical for a variety of cognitive functions such as sensory processing (Fries et al., 2001), memory (Fernández-Ruiz et al., 2021), navigation (Colgin et al., 2009), and conscious awareness (Rodriguez et al., 1999). At the cellular scale, gamma rhythms modulate spiking activity, shaping the formation of transient neuronal partnerships, the so-called cell assemblies (Buzsáki, 2010). Computational models show that gamma depends on local inhibitory-inhibitory or excitatory-inhibitory interactions (Tort et al., 2007; Wang and Rinzel, 1992) and ultimately emerges from synchronous inhibitory postsynaptic potentials (Buzsáki and Wang, 2012). However, despite the initial evidence for their underlying principles being general, gamma oscillations are not a monolithic entity but actually encompass a diversity of rhythms observed experimentally (Lopes-Dos-Santos et al., 2018; Scheffer-Teixeira et al., 2012; Schomburg et al., 2014; Zhong et al., 2017). This warrants studying the mechanisms and functions of these oscillations in specific brain regions *in vivo.*

Gamma oscillations usually appear nested within slower rhythms, a phenomenon known as cross-frequency coupling, in which the amplitude of gamma waxes and wanes depending on the phase of a slow oscillation (Canolty and Knight, 2010; Lisman and Jensen, 2013). Important examples are the coupling of specific gamma sub-bands to the hippocampal theta rhythm (Cavelli et al., 2020; Sirota et al., 2008; Tort et al., 2008, 2009) or to the phase of breathing cycles (Cavelli et al., 2018; Ito et al., 2014; Zhong et al., 2017). Regarding the latter, it is worth noting that respiration-entrained brain rhythms depend on nasal airflow and are not a consequence of the respiratory pattern generation in the brainstem (Lockmann et al., 2016; Moberly et al., 2018; Yanovsky et al., 2014). Therefore, it seems likely that

respiration-entrained gamma activity arises from local computations driven by sensory inputs sampled at each breath and thus plays a major role in cognition. In close agreement with these ideas, the piriform (olfactory) cortex (PCx) shows prominent gamma oscillations modulated by breathing patterns and olfactory information (Bressler and Freeman, 1980; Freeman, 1960; Freeman and Skarda, 1985; Vanderwolf, 2000). But despite being reported since 1960, the mechanisms and functions of gamma oscillations in the PCx remain controversial (Bressler, 1988; Courtiol et al., 2019; Freeman, 1960; Vanderwolf, 2000; Zibrowski and Vanderwolf, 1997).

In this report, we study gamma oscillations in the PCx of the awake mouse. We took advantage of modern genetic tools that modify the local connectivity and dynamics of the PCx, enabling the study of the mechanisms and functions of its oscillatory activity. We found that respiration drives inhibitory gamma oscillations in this region, which depend on recurrent connections between local excitatory and inhibitory populations. This loop is triggered by the projection of mitral/tufted cells in the olfactory bulb onto principal cells of the PCx. As functional consequences, we show that respiration-driven gamma oscillations determine odor-assembly representations through a winner-take-all computation taking place within breathing cycles.

Results

Respiration drives inhibitory gamma oscillations in the piriform cortex

To understand the mechanisms and functions of gamma oscillations and their relationship with respiration in the mouse brain, we analyzed local field potentials (LFP) from the PCx recorded simultaneously with the respiration signal (Fig 1A). Figure 1B depicts the LFP and respiration signal from a representative animal; notice that low-gamma oscillations (30-60 Hz) emerge ~100 ms following inhalation start. These low-gamma oscillations, already evident in raw recordings, are part of a larger gamma peak (30-100 Hz) in the LFP power spectrum (Fig 1C), reflecting a true oscillation (Yuval-Greenberg et al., 2008). Consistent with Figure 1B, only the low-gamma sub-band couples to the respiration cycle across animals, as its amplitude is modulated by both a 2-3 Hz LFP rhythm coherent to respiration (Fig 1D top panel; see also Figs S1 and S2) and by respiration itself (Fig 1D bottom panel). Thus, respiration entrains low-gamma oscillations in the PCx.

We analyzed the contribution of the different PCx neuronal populations to network low-gamma oscillations by first classifying single units according to the expression of a light-sensitive channelrhodopsin coupled to the vesicular GABA transporter (VGAT). This allowed to discriminate between VGAT- principal cells and VGAT+ inhibitory interneurons. Additionally, VGAT+ neurons were further classified into feedback inhibitory interneurons (FBI) according to their location relative to the principal cell layer (FBI tend to be located at a more superficial level within the cell layer 2/3; Bolding and Franks, 2018). Upon averaging the activity of each neuronal subpopulation, we found that the time-course of FBI firing rate changes correlates with the amplitude of low-gamma oscillations in both time and respiratory phase (Fig 1E). In contrast, principal cells spike earlier within the respiratory cycle and return to baseline during the gamma amplitude peak (Fig 1E). Therefore, we conclude that respiration-entrained low-gamma oscillations in the PCx are inhibitory.

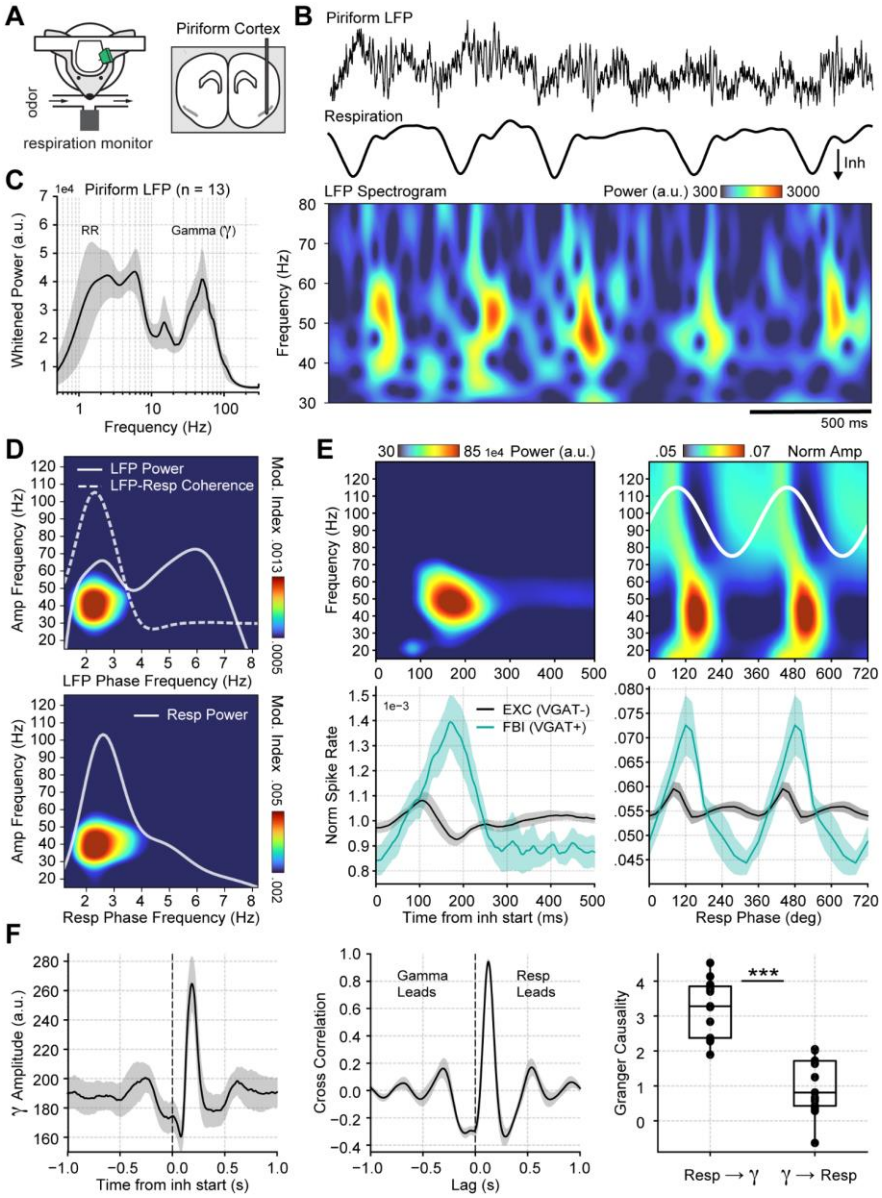

Fig 1. Respiration drives inhibitory gamma oscillations in the piriform cortex.
A Experimental scheme and probe localization (modified from Bolding and Franks, 2018). **B** Example of simultaneously recorded LFP (top) and respiration (middle) signals, along with the LFP wavelet spectrogram (bottom). Notice prominent rhythmical appearance of gamma oscillations. **C** Average LFP power spectrum (± 2*SEM). The spectrum was whitened by multiplying each value by the associated frequency. **D** Average phase-amplitude comodulogram using either the LFP (top) or the respiration (Resp; bottom) phase. Superimposed white lines show the LFP or Resp power spectrum (solid) and the LFP-Resp coherence (dashed). **E** Respiration-evoked LFP responses. Top: inhalation-triggered spectrogram (left) and normalized amplitude for LFP-filtered frequency components as a function of the Resp phase (right). Bottom: Spike rate (mean ± SEM) of excitatory (EXC; VGAT-) and feedback inhibitory (FBI; VGAT+) neuronal populations triggered by inhalation (left) or binned by the Resp phase (right). **F** Directionality analyses between Resp and the gamma envelope (30-60 Hz). Shown are the average (± SEM) gamma envelope triggered by inhalation start (left), the average (± SEM) cross-correlation between Resp and the gamma envelope (middle), and the Granger causality for the Resp→gamma and gamma→Resp directions (right; boxplots show the median, 1st, 3rd quartiles, and the distribution range; each dot shows an individual mouse).

To further characterize the interaction between respiration and low-gamma oscillations in the PCx, we performed directionality analyses (Fig 1F). The gamma amplitude envelope showed a peak ~200 ms following the inhalation start, coinciding with a large positive cross-correlation peak between these signals, which suggests that respiration causes gamma. Consistent with these results, time-domain Granger causality was significantly higher in the respiration→gamma direction than in the opposite one ($t(12) = 9.28$, $p<10^{-6}$). Together, these results show that respiration drives inhibitory low-gamma oscillations in the PCx.

Respiration-driven gamma oscillations depend on recurrent connections within the piriform cortex

We next studied the circuit mechanisms responsible for the respiration-driven gamma oscillations in the PCx. To that end, we analyzed PCx LFPs following the selective expression of the tetanus toxin light chain in principal cells of a targeted hemisphere (TeLC ipsi; Fig 2A). Under this approach, TeLC expression blocks excitatory synaptic transmission without affecting cellular excitability (Bolding and Franks, 2018), allowing us to study the local computations underlying the respiration-driven gamma. Figure 2B shows that TeLC ipsi LFPs had a large significant reduction in low-gamma oscillations with respect to either control mice ($t(19) = 4.59$, $p<0.0001$) or the contralateral PCx (TeLC contra, not infected; $t(12) = 3.79$, $p = 0.0012$). Moreover, TeLC ipsi LFPs also showed a significant decrease in respiration-gamma coupling compared to control ($t(19) = 10.52$, $p<10^{-8}$) or TeLC contra LFPs ($t(12) = 2.78$, $p = 0.008$) (Fig 2C,D), despite the respiration signal still reaching the PCx (note the dotted white traces in Fig 2C showing LFP-Resp coherence). These results demonstrate that gamma oscillations and their coupling to respiration depend on local recurrent excitatory connections within the PCx.

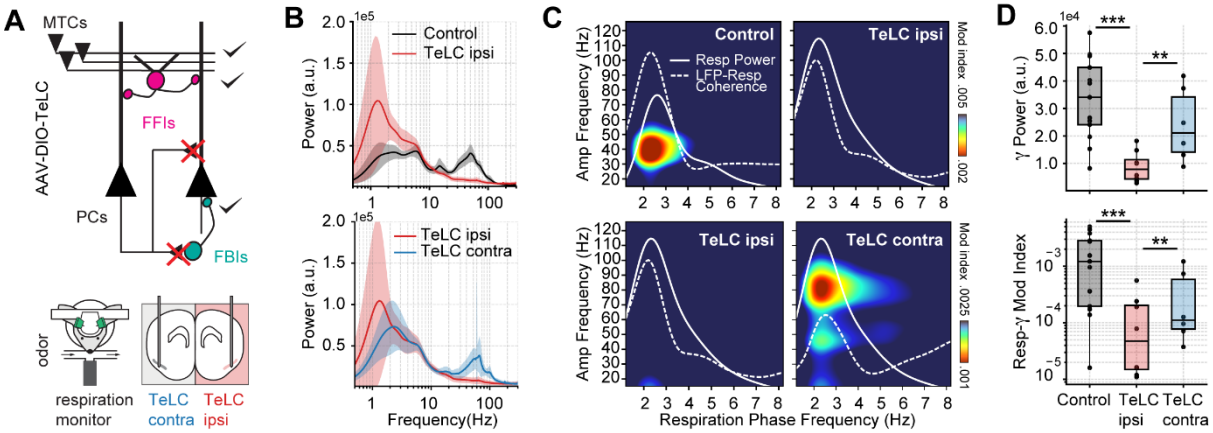

Fig 2. Respiration-driven gamma oscillations depend on recurrent connections within the piriform cortex. A Schematic of circuit changes after TeLC expression in principal cells (PCs) of the piriform circuit (MTCs: mitral cells; FFIs: feedforward interneurons; FBIs: feedback interneurons). Recordings were made both ipsi- and contralaterally to the TeLC expression (modified from Bolding and Franks, 2018). **B** Average (± 2*SEM) power spectra for control and TeLC-infected animals. Notice that local TeLC expression abolishes ipsilateral gamma oscillations in the PCx. **C** Average respiration-LFP comodulograms for control and TeLC-infected animals. Respiration power and LFP-respiration coherence are shown superimposed (same scale across plots). **D** Boxplots showing gamma power (top) and the Resp-low gamma modulation index (bottom) for control and TeLC-infected animals.

Olfactory bulb mitral-cell projections trigger recurrent gamma oscillations in the piriform cortex

After confirming that respiration-driven gamma oscillations depend on recurrent connections formed by principal cells, we asked how PCx inputs affect gamma generation. We expected mitral/tufted cell activation in the olfactory bulb (OB) to trigger similar low-gamma oscillations since these projections convey the respiratory inputs to the PCx (Pashkovski et al., 2020). Consistently, optogenetic activation of the OB (Thy-Control) triggered piriform low-gamma oscillations, which matched the laser time-course (Fig 3A, top panel). Interestingly, TeLC ipsi LFPs showed almost no gamma activity following laser onset (Fig 3A, middle panel), while TeLC contra LFPs still exhibited gamma activity upon stimulation of the OB (Fig 3A, bottom panel). Analyzing the group response, we found a significant reduction of low-gamma activity following the laser onset in TeLC ipsi LFPs compared to control ($t(4) = 4.98$, $p<0.0001$) or TeLC contra LFPs ($t(6) = 3.49$, $p = 0.0012$) (Fig 3B,C), further confirming the importance of recurrent connections for gamma generation. Moreover, low-gamma power in control and TeLC contra LFPs increased with laser intensity, while it remained constant in TeLC ipsi LFPs (Fig 3D). In summary, the results show that respiration drives PCx low-gamma oscillations mediated by OB projections from mitral/tufted cells.

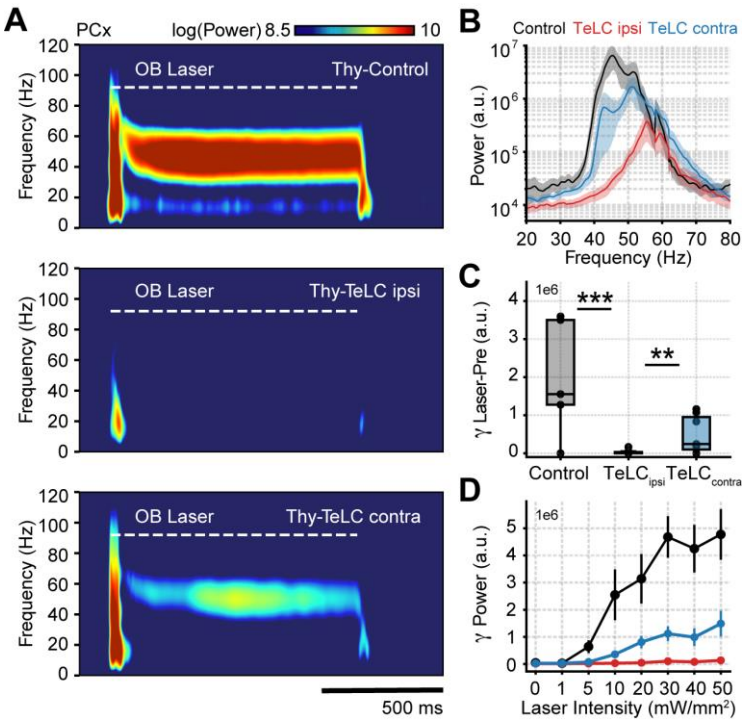

Fig 3. Olfactory bulb projections trigger recurrent low-gamma oscillations in the piriform cortex.
A Average PCx spectrograms triggered by optogenetic stimulation of the olfactory bulb (OB). **B** Average gamma power during OB stimulation for the control, TeLC ipsi and contralateral recordings. **C** Boxplots showing the gamma power difference between the laser and pre-laser periods. **D** Gamma power as a function of the laser intensity for each experimental condition (mean ± SEM).

Respiration-driven gamma oscillations determine odor-assembly representations through a winner-take-all computation

Finally, having revealed the mechanisms of respiration-driven low-gamma oscillations in awake mice, we next studied their relationship to olfaction. Noteworthy, respiration-driven low gamma oscillations depended on the cognitive state since ketamine/xylazine anesthesia abolished them (Fig S3). First, we compared the average gamma responses of the odorless respiratory cycles against the cycles in which an odorant was presented. We found that odor delivery elicits longer-lasting gamma oscillations, though with similar peak amplitude and peak latency within respiratory cycles (Fig 4A). Interestingly, odor delivery led to prolonged breaths; however, the longer respiratory cycle could not account for the prolonged gamma activity during odor sampling since no such effect was observed in odorless cycles matching odor breathing frequency (Fig S4).

Further analyses revealed that the piriform low-gamma activity did not depend on odor identity (Fig 4A), changed slightly with odor concentration (Fig S5), and required recurrent piriform connectivity (Fig S6). In contrast, beta oscillations, previously related to olfaction (Lepousez and Lledo, 2013; Martin et al., 2006; Poo and Isaacson, 2009), greatly increased during odor presentation (Fig S6). Nevertheless, as opposed to low-gamma which were induced at each respiratory cycle, beta oscillations were evoked and, moreover, still present in TeLC animals (Fig S6), suggesting they do not relate to local activity and are likely of postsynaptic origin (for a discussion about evoked vs. induced oscillations, see Tallon-Baudry and Bertrand, 1999). Therefore, these observations suggest that gamma oscillations reflect a common local computation orchestrating olfactory spiking.

Next, we studied how gamma oscillations influence principal cell spiking, pooling together all recorded principal cells and analyzing their spiking as a function of the respiration phase. We found that the respiration phase modulated principal cell spiking within breathing cycles (Fig 4B), though the preferred spiking phase differed across neurons. Interestingly, while a large proportion of cells were inhibited during the same respiration phase as the maximal gamma amplitude, some cells increased their spiking coincidently with the gamma peak. Importantly, the cells with increased spikes during gamma depended on odor context: when analyzing the population response to six different odorants (0.3% v./v. concentration), we found a noticeable cell-odor gamma spike specificity, that is, some cells spiked during gamma for a particular smell and not for the others (Fig 4C).

The gamma spiking specificity supports the conjecture that respiration-driven gamma oscillations could mediate odor assembly representations. To further study this possibility, we analyzed cell-assembly compositions for each odor by measuring the contribution of each principal cell to the first principal component (PC) of the population response (El-Gaby et al., 2021; Lopes-dos-Santos et al., 2013; Trouche et al., 2016). For each odor, we found that only a small fraction of neurons showed a strong positive contribution to the 1st PC, thereafter referred to as winner cells, while the vast majority showed low negative weights (Fig 4D,E), referred to as loser cells. Notably, the few winning neurons determining the 1st PC activity changed from odor to odor (Fig 4C,D); in other words, there was strong orthogonality in the 1st PC weight distribution across different odors. Consistent with this, the 1st PC weights were not significantly correlated between odors ($p>0.016$, corrected by multiple comparisons) (Fig 4F). Interestingly, the losing cells were significantly more phase-

locked to the gamma phase (Fig 4G), consistent with these being actively inhibited by the oscillation. Moreover, when analyzing the spiking time-course of winner and loser cells, we found that both groups tended to spike immediately following inhalation start; nevertheless, once feedback inhibition was recruited, loser cells spiked below their average while the winner cells continued spiking above baseline (Fig 4H). Thus, these results suggest that sparse odor assembly representations emerge from a winner-take-all process mediated by inhibitory gamma oscillations.

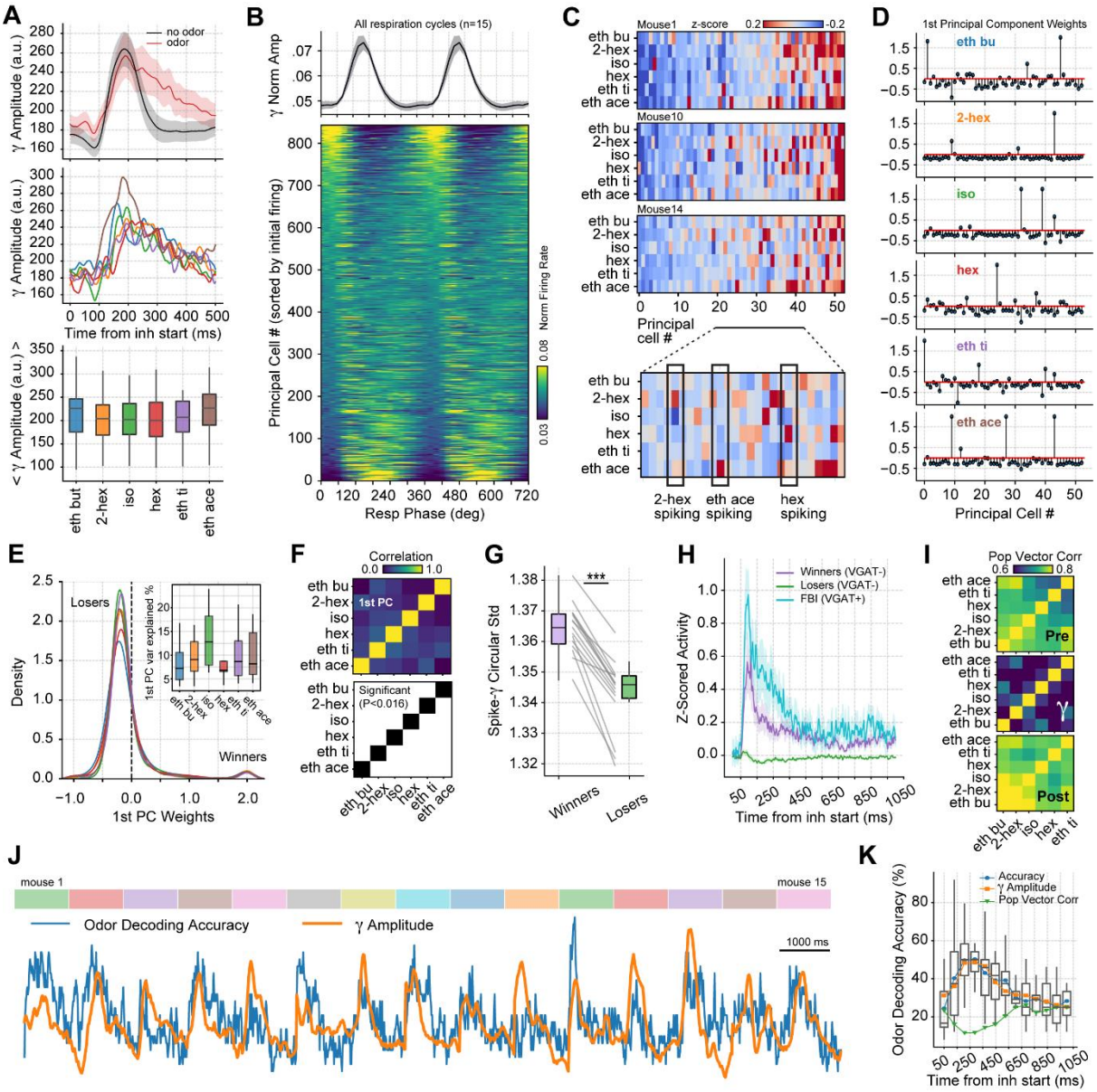

Fig 4. Respiration-driven gamma oscillations determine odor-assembly representations through a winner-take-all computation.

A Top: Induced gamma amplitude triggered by the inhalation start. Shown are the average gamma response to odorless respiratory cycles and cycles containing odor sampling. Middle: Average gamma amplitude for six different odorants. Bottom: Boxplots showing the mean gamma amplitude for the different odorants. **B** Principal cell spiking during each phase bin of the respiration cycle (bottom; 0 degree corresponds to the start of the inhalation); neurons are sorted according to the normalized firing rate in the first bin. Gamma power is shown on top (mean ± SEM). **C** Z-scored firing rate at the gamma peak in response to different odors for 3 representative mice. For each mouse, columns show

the firing rates for the same principal cell. The bottom panel shows a zoom-in view of a representative differential spiking activity across odors. **D** Assembly weights for the 1st principal component (1st PC) in a representative mouse during the presentation of odorants. Notice different assembly compositions for the different odors. **E** Distribution of assembly weights for the 1st PC of each odor (all principal cell weights across sessions pooled together). Inset: % of variance explained by the 1st PC. **F** Correlation among 1st PC weights. The bottom panel shows the correlation statistics (thresholded at 0.016 according to the Bonferroni correction for multiple comparisons; black: statistically significant; white = non-significant). **G** Boxplots showing the circular standard deviation of the spiking gamma phase for winning and losing neurons. **H** Average z-scored spiking activity for winners, losers and feedback inhibitory neurons. **I** Population vector correlations between odor responses during 100-ms time windows before (Pre), during (Gamma) and after (Post) the gamma peak. Only principal cells were employed for this analysis. **J** Odor decoding accuracy (blue) and gamma amplitude (orange) time-courses for each mouse (individual data following inhalation start were concatenated for representation purposes). **K** Boxplots showing odor decoding accuracy following inhalation start employing 100-ms time bins. The mean accuracy across mice is shown by the blue line; for comparisons, the orange line shows the average gamma amplitude (arbitrary scale) and the green line shows the population vector correlations between principal cells (see Methods).

Because a winner-take-all process selects a single odor representation while actively suppressing others, it effectively implements an XOR logic gate. As a consequence, we would expect odor decoding accuracy to increase during gamma inhibition. Following this reasoning, we first analyzed the correlation of population spiking vectors in response to different odorants and found that correlations significantly dropped during the gamma peak (Pre vs. Gamma: $t(14) = 3.93$, $p = 0.0007$; Gamma vs. Post: $t(14) = 4.95$, $p = 0.0001$; Fig 4I), confirming that odor representations diverge the most during gamma inhibition. We next tested odor decoding from the principal cell activity by training a supervised linear classifier using population spiking (i.e., spike vectors) at different respiratory cycle phases. Consistent with a winner-take-all mechanism, we found that variations in odor decoding accuracy matched the low-gamma activity time-course (Fig 4J); there was significant correlation between these variables ($r = 0.47$, $p<10^{-63}$). Importantly, decoding accuracy significantly increased around the gamma peak compared to time windows before or after it (Pre vs. Gamma: $t(14) = 5.52$, $p<0.0001$; Gamma vs. Post: $t(14) = 7.47$, $p<10^{-5}$, Fig S7; see also Fig 4K). This result was robust among different classification algorithms (Fig S7), confirming that gamma inhibition generates a sparse PCx representation during odor processing. These results thus demonstrate that respiration-driven gamma oscillations provide an optimal temporal window for olfaction.

Discussion

The present report unveils the mechanisms and functions of gamma oscillations in the PCx of awake mice. We show that respiratory inputs to this cortex elicit large feedback inhibitory low-gamma oscillations that aid odor coding. Our work provides crucial details for understanding gamma oscillations in the olfactory system. First, our results support the excitatory-inhibitory models of gamma generation (Buzsáki and Wang, 2012; Fisahn et al., 1998), highlighting the role of excitatory neurons in initiating the gamma cycle by driving feedback interneuron spiking, similar to the mechanisms generating gamma in the olfactory bulb (Lepousez and Lledo, 2013). Second, we demonstrate that these low-gamma oscillations are the extracellular correlates of a winner-take-all process, thus confirming previous theoretical conjectures (de Almeida et al., 2009) and linking this brain oscillation to

an algorithmic operation (an XOR logic gate). Third, the winner-take-all interpretation provides a direct relationship between gamma oscillations and cell assemblies. Under this scenario, the low-gamma feedback inhibition is critical for segregating cell assemblies and generating a sparse, orthogonal odor representation. Concomitantly, the assembly recruitment would depend on excitatory-excitatory interactions among winner cells during gamma activity.

An important feature of the respiration-driven low-gamma oscillations is that the winners triggering them change according to odor context (Fig 4C). Thus, the involvement of different cells and spiking dynamics likely makes the recruitment of feedback inhibition a non-homogenous process across respiration cycles, leading to small time jitters in peak gamma activity. As an empirical end result, the observed low-gamma oscillations are not phase-locked from cycle to cycle; in other words, PCx low-gamma power is induced, but not evoked (Tallon-Baudry and Bertrand, 1999), at each respiratory cycle. In contrast, beta oscillations were evoked by the respiratory input to the PCx, leading to a prominent phase resetting ~100 ms after the inhalation start (Fig S6). Further consistent with these results, respiration-triggered beta oscillations did not disappear in the TeLC condition and correlated in time with excitatory spiking (c.f. Fig S6 and Fig 1). Interestingly, a previous report showed that odors evoke PCx beta oscillations under urethane anesthesia (Poo and Isaacson, 2009) here (Fig S6), occurred before global inhibition (Poo and Isaacson 2009). Based on this, a role for piriform beta in odor representations has been proposed; nevertheless, here we show that beta oscillations are likely inherited and do not require local computations in the PCx, i.e., they are not locally generated. In contrast, our results demonstrate that the piriform gamma does arise locally (and are not present during anesthesia), suggesting that odor coding ultimately depends on low-gamma oscillations in the main olfactory cortex of the mouse.

The study of the role of the PCx in olfaction has recently been boosted by selective genetic techniques, allowing researchers to examine how the individual cellular components relate to olfaction (Franks et al., 2011; Nagappan and Franks, 2021). The PCx, also known as the olfactory cortex, receives inputs from the OB and constructs a robust odor representation (Bolding et al., 2020). This representation can be inferred from the population activity and has two major features. On the one hand, it separates odor identity from its concentration (Bolding and Franks, 2017, 2018; Roland et al., 2017). This process depends on large-scale piriform inhibition (Bolding and Franks, 2018) and thus correlates with low-gamma oscillations. On the other hand, the representation groups odors into perceptual categories, not necessarily related to the physical structure of the odor molecules (Pashkovski et al., 2020). We hypothesize that low-gamma oscillations provide a critical time window for odor assembly representations to be formed and modified through winner-take-all computations. Our decoding analysis supports this idea by showing that, for a reader neuron, the optimal odor decoding occurs during the peak gamma activity within breathing cycles. Interestingly, and further consistent with these results, a recent study in humans showed that the accurate perception and identification of odors depend on piriform gamma oscillations (Yang et al., 2022). Moreover, the behavioral response to odors also seems to depend on piriform gamma, and its suppression induces depressive-like behaviors in mice (Li et al., 2022).

Several reports show that the PCx is the source of gamma activity for widespread brain regions, including the striatum (Carmichael et al., 2017) and the anterior limbic system (Carmichael et al., 2019). Although the authors largely attribute such oscillations to piriform

volume conduction, recent evidence shows that olfactory gamma synchronizes distant regions as well (Li et al., 2022). Based on our results, we postulate that genuine respiration-entrained gamma oscillations in downstream regions are triggered by the output of the winning piriform assemblies, leading to new local gamma winner-take-all processes. This provides a new look into long-range gamma synchronization, emerging naturally if winners generating gamma in one area consistently trigger winners generating gamma in a downstream area. In accordance with our results, a recent report showed that respiration-related brain oscillations drive sparse assemblies in the prefrontal cortex (Folschweiller and Sauer, 2022). Moreover, these authors also found that inhibitory recruitment by assembly members was key for assembly segregation. In all, the directional view of synchronization across regions places a major role in cross-frequency interactions driving communication, highlighting the relevance of interregional synchrony modulation by slower rhythms, for instance theta (González et al., 2020) or respiration itself (Cavelli et al., 2020)**.**

In summary, we have shown that respiration drives feedback inhibitory low-gamma oscillations in the PCx, which determine sparse odor-assembly representations through a winner-take-all computation on a respiratory cycle-by-cycle basis. Our results shed new light on the mechanisms of gamma oscillations, their coupling to respiration, and their computational role in olfaction.

Methods

Datasets

We analyzed recordings of the PCx generously made available by Bolding and Franks through the Collaborative Research in Computational Neuroscience data sharing website (http://crcns.org, pcx-1 dataset). Detailed descriptions of the experimental procedures can be found in previous publications (Bolding and Franks, 2017, 2018; Bolding et al., 2020). All protocols were approved by the Institutional Animal Care and Use Committee of Duke University. Below we describe the analytical methods employed by us, and, for convenience, also the relevant experimental procedures from the original publications.

Animals

Adult mice were employed (>P60, 20-24 g), housed in single cages on a normal light-dark cycle. For the Cre-dependent TeLC group, offspring of Emx1-cre (+/+) breeding pairs were obtained from The Jackson Laboratory (005628). For the optogenetic experiments, the mice employed were: adult Thy1-ChR2-YFP (+/+), line 18 (Thy1-COP4/EYFP, Jackson Laboratory, 007612) and VGAT-ChR2-YFP (+/−), line 8 (Slc32a1-COP4*H134R/EYFP, Jackson Laboratory, 014548). For the combined optogenetics and TeLC expression experiments, adult offspring of Emx1-cre (+/+) mice crossed with Thy1-ChR2-YFP (+/+) mice were employed.

Adeno-associated viral vectors

For the TeLC experiments, AAV5-DIO-TeLC-GFP was expressed under CBA control (6/7 mice) or synapsin (1/7 mice), whose effects were similar and pooled together. Three 500 nL injections in the PCx (AP, ML, DV: +1.8, 2.7, 3.85; +0.5, 3.5, 3.8; -1.5, 3.9, 4.2; DV

measured from brain surface) were employed to achieve TeLC expression. All recordings took place ~14 days after the promoter injection. All viruses were obtained from the University of North Carolina-Chapel Hill (UNC Vector Core)

Data acquisition

The electrophysiological signals were recorded using 32-site polytrode acute probes (A1x32-Poly3-5mm- 25s-177, Neuronexus) with an A32-OM32 adaptor (Neuronexus) through a Cereplex digital headstage (Blackrock Microsystems). For the optogenetic identification of GABAergic cells, a fiber-attached polytrode probe was employed (A1x32-Poly3-5mm-25s-177-OA32LP, Neuronexus). Data was acquired at 30 kHz, unfiltered, employing a Cerebus multichannel data acquisition system (BlackRock Microsystems). Respiration and experimental events were acquired at 2 kHz by analog inputs of the Cerebus system. The respiration signal was measured employing a microbridge mass airflow sensor (Honeywell AWM3300V), which was positioned opposite to the animal nose. Inhalation generated a negative airflow and thus negative changes in the voltage of the sensor output.

Electrode and optic fiber placement

A Patchstar Micromanipulator (Scientifica) was employed to position the recording probe in the anterior PCx (1.32 mm anterior and 3.8 mm lateral from bregma). Recordings were targeted 3.5–4 mm ventral from the brain surface at this position, and were further adjusted according to the LFP and spiking activity monitored online. The electrode sites spanned 275 µm along the dorsal-ventral axis. The probe was lowered until an intense spiking band was found, which covered 30–40% of electrode sites near the correct ventral coordinate, thus reflecting the piriform layer II. For the optogenetic experiments stimulating OB cells in Thy1-ChR2-YFP mice, the optic fiber was placed <500 µm above the OB dorsal surface.

Spike sorting and waveform characteristics

Spyking-Circus software was employed to isolate individual units (https://github.com/spyking-circus). All clusters which had more than 1% of ISIs violating the refractory period (< 2 ms) or appearing contaminated were manually removed. Units which showed both similar waveforms and coordinated refractory periods were merged into a single cluster. The unit position was characterized as the mean electrode position (across electrodes) weighted by the amplitude of the unit waveform on each electrode.

Analytical Methods

For all analyses, we used Python 3 with numpy (https://numpy.org/), scipy (https://docs.scipy.org/), matplotlib (https://matplotlib.org/), sklearn (https://scikit-learn.org/stable/) and statsmodel (https://www.statsmodels.org/stable/index.html) libraries.

Preprocessing

Raw LFPs were decimated to a sampling rate of 2000 Hz to match the respiration signal sampling rate, employing the *decimate* scipy function. This function first low-pass filters the 30 kHz raw data and then downsamples it, avoiding aliasing. For each animal, we used the

same channel (channel 16, located in the middle of the probe) for all analyses, though similar results are obtained for the rest of the channels given their high LFP redundancy (Fig S8).

Power spectrum

To analyze the LFP spectra, we computed Welch's modified periodogram using *welch* scipy function. Specifically, we employed a 1-s moving window with half a window overlap, setting the frequency resolution to 0.1 Hz. All spectra were whitened by multiplying each power value by its associated frequency, thus eliminating the 1/f trend. For Figure 1B, we computed the wavelet transform (*cwt* scipy function) of the LFP signal using a Morlet wavelet with 0.1 Hz resolution.

The triggered spectrograms were obtained first selecting all 500-ms LFP windows following inhalation start (time stamps provided in the dataset, see Bolding and Franks 2018 for further details) and then computing the spectrogram using the *spectrogram* scipy function. We used 100-ms windows with 90% overlap and a frequency resolution of 0.1 Hz. After computing each individual spectrogram, we averaged them to yield the mean spectrogram shown in Figures 1E and 3A.

Phase-amplitude coupling

We computed phase-amplitude comodulograms following the methods proposed by (Tort et al., 2010). We first band-pass filtered the LFP/respiration signal using the *eegfilt* function (Delorme and Makeig, 2004) adapted for Python 3 (available at github/joaqgonzar). We filtered between 20 to 130 Hz in 10-Hz steps to obtain the higher frequency components, and between 1 and 8 Hz in 1-Hz steps to obtain the slower frequency components. The phase (angle) and amplitude time series of the filtered signals were estimated from their analytical representation based on the Hilbert transform. We then binned the phase time-series into 18 bins and computed the mean amplitude of the fast signal for each bin. The amount of phase-amplitude coupling was estimated through the modulation index (MI) metric (Tort et al., 2010), MI = (Hmax-H)/Hmax, where Hmax is the maximum possible Shannon entropy for a given distribution (log(number of phase bins)) and H is the actual entropy of the amplitude distribution.

Individual cell spiking responses to inhalation

We convolved the spike times of each unit with a 20-ms Gaussian kernel (standard deviation of 5 ms) employing the *convolve* scipy function. For each animal, the spiking response of a neuronal subpopulation (i.e., excitatory or FBI neurons) was normalized by dividing the average firing rate by its sum across time [phase] bins; in Figure 1E, the results show the mean ± SEM across animals.

Directionality analysis

To study the directionality between the gamma envelope and respiration signal, we employed three different strategies: (1) we averaged the gamma envelope using the inhalation start as a trigger; (2) we computed the cross-correlogram, using the *correlate*

scipy function, between the gamma envelope and the respiration signal; (3) we computed Granger Causality estimates, using the *grangercausalitytest* stats model function, with a 10-order VAR model and employing the log(F-stat) as the Granger Causality magnitude (Geweke, 1982).

Principal component analysis

We employed the *PCA* sklearn function on concatenated time-series of the smoothed principal cell spiking activity using all 1000-ms windows following inhalation start during odor presentation. Each odor was treated separately. We analyzed only the first principal component, explaining the most variance, setting n_components = 1. Winners and losers were identified according to the weight each neuron exerted on the 1st principal component. Namely, neurons with a positive weight were labeled as winners and neurons with a negative weight as losers.

Gamma phase-locking

To assess coupling between spikes and gamma phase, the circular standard deviation of the spiking gamma phases was calculated using the *scipy circstd* function.

Population vector correlations

To infer the similarity/dissimilarity in the population response to the different odors, we analyzed the population vector correlations, defined as the Pearson correlation (*pearsonr* scipy function) measured using paired data from the same neurons to two odors. Correlations were computed between spiking vectors for each odor; the correlation time course shown in Figure 4K was obtained using 100-ms sliding windows (87.5% overlap) following inhalation start. For statistics, we averaged the correlation across odors and compared them among 3 time windows of interest (see Fig 4I): from 0-100 ms (Pre), from 150-250 ms (Gamma), and from 875-975 ms (Post).

Odor decoding

We employed a supervised linear classifier to decode the odor stimulus from the population spiking vectors. The classification algorithm was supplied with the average spiking of each principal cell in 100-ms sliding windows following the inhalation start. The classification algorithm was a linear support vector machine with a stochastic gradient descent optimization, implemented using the *sgdclassifier* sklearn function. Each mouse was trained and tested separately; the training sample consisted of 2/3 of the data, and the test sample consisted of the remaining third. The division of training/test samples was randomized in order to avoid odor bias. For the statistical comparisons, we used the same 100-ms time windows employed in the population vector correlations (i.e., Pre, Gamma, and Post). To verify the robustness of the results, we also employed a linear discriminant analysis and a k-nearest neighbor classifier, which rendered similar results to the sgdclassifier algorithm (Fig S7).

Statistics

We show data as either mean ± SEM or regular boxplots showing the median, 1st, 3rd quartiles and the distribution range without outliers. We employed paired and unpaired t-test to compare between groups. We set $p<0.05$ to be considered significant (in the figure panels, *, ** and *** denote $p<0.05$, $p<0.01$ and $p<0.001$, respectively). For the population vector correlations as well as 1st PC weight correlations, we employed Pearson r correlation and corrected the statistical threshold through the Bonferroni method for multiple comparisons ($p<0.016$).

Code and data availability

All the data employed is freely available at: http://crcns.org, pcx-1 dataset. All of the analysis routines are available upon request to the first author.

Acknowledgments

We thank Kevin Bolding and Kevin Franks for making their data available and for insightful comments on our manuscript. We also thank Diego Laplagne for comments on the manuscript. JG was supported by Comision Academica de Posgrado (CAP), Programa de Desarrollo de Ciencias Básicas (PEDECIBA) and Comisión Sectorial de Investigación Científica (CSIC). PT was supported by PEDECIBA and CSIC. ABLT was supported by Conselho Nacional de Desenvolvimento Científico e Tecnológico (CNPq) and Coordenação de Aperfeiçoamento de Pessoal de Nível Superior (CAPES), Brazil.

Author contributions

JG conceptualized the work, created and implemented all of the analysis routines and wrote the initial manuscript. PT and ABLT supervised all the stages of this work and suggested analysis directions. All authors wrote the final manuscript.

Conflict of interest

The authors declare no conflict of interest

References

Adrian, E.D. (1942). Olfactory reactions in the brain of the hedgehog. J. Physiol. *100*, 459–473.

de Almeida, L., Idiart, M., and Lisman, J.E. (2009). A second function of gamma frequency oscillations: an E%-max winner-take-all mechanism selects which cells fire. J. Neurosci. *29*, 7497–7503.

Bolding, K.A., and Franks, K.M. (2017). Complementary codes for odor identity and intensity in olfactory cortex. Elife *6*.

Bolding, K.A., and Franks, K.M. (2018). Recurrent cortical circuits implement concentration-invariant odor coding. Science *361*.

Bolding, K.A., Nagappan, S., Han, B.-X., Wang, F., and Franks, K.M. (2020). Recurrent circuitry is required to stabilize piriform cortex odor representations across brain states. Elife *9*.

Bragin, A., Jandó, G., Nádasdy, Z., Hetke, J., Wise, K., and Buzsáki, G. (1995). Gamma (40-100 Hz) oscillation in the hippocampus of the behaving rat. J. Neurosci. *15*, 47–60.

Bressler, S.L. (1988). Changes in electrical activity of rabbit olfactory bulb and cortex to conditioned odor stimulation. Behav. Neurosci. *102*, 740–747.

Bressler, S.L., and Freeman, W.J. (1980). Frequency analysis of olfactory system EEG in cat, rabbit, and rat. Electroencephalogr. Clin. Neurophysiol. *50*, 19–24.

Buzsáki, G. (2010). Neural syntax: cell assemblies, synapsembles, and readers. Neuron *68*, 362–385.

Buzsáki, G., and Wang, X.-J. (2012). Mechanisms of gamma oscillations. Annu. Rev. Neurosci. *35*, 203–225.

Canolty, R.T., and Knight, R.T. (2010). The functional role of cross-frequency coupling. Trends Cogn. Sci. *14*, 506–515.

Carmichael, J.E., Gmaz, J.M., and van der Meer, M.A.A. (2017). Gamma Oscillations in the Rat Ventral Striatum Originate in the Piriform Cortex. J. Neurosci. *37*, 7962–7974.

Carmichael, J.E., Yuen, M.M., and van der Meer, M.A.A. (2019). Piriform cortex provides a dominant gamma LFP oscillation in the anterior limbic system.

Cavelli, M., Rojas-Líbano, D., Schwarzkopf, N., Castro-Zaballa, S., Gonzalez, J., Mondino, A., Santana, N., Benedetto, L., Falconi, A., and Torterolo, P. (2018). Power and coherence of cortical high-frequency oscillations during wakefulness and sleep. Eur. J. Neurosci. *48*, 2728–2737.

Cavelli, M., Castro-Zaballa, S., Gonzalez, J., Rojas-Líbano, D., Rubido, N., Velásquez, N., and Torterolo, P. (2020). Nasal respiration entrains neocortical long-range gamma coherence during wakefulness. Eur. J. Neurosci. *51*, 1463–1477.

Colgin, L.L., Denninger, T., Fyhn, M., Hafting, T., Bonnevie, T., Jensen, O., Moser, M.-B., and Moser, E.I. (2009). Frequency of gamma oscillations routes flow of information in the hippocampus. Nature *462*, 353–357.

Courtiol, E., Buonviso, N., and Litaudon, P. (2019). Odorant features differentially modulate beta/gamma oscillatory patterns in anterior versus posterior piriform cortex. Neuroscience *409*, 26–34.

Csicsvari, J., Jamieson, B., Wise, K.D., and Buzsáki, G. (2003). Mechanisms of gamma oscillations in the hippocampus of the behaving rat. Neuron *37*, 311–322.

Delorme, A., and Makeig, S. (2004). EEGLAB: an open source toolbox for analysis of single-trial EEG dynamics including independent component analysis. J. Neurosci. Methods *134*, 9–21.

El-Gaby, M., Reeve, H.M., Lopes-Dos-Santos, V., Campo-Urriza, N., Perestenko, P.V., Morley, A., Strickland, L.A.M., Lukács, I.P., Paulsen, O., and Dupret, D. (2021). An emergent neural coactivity code for dynamic memory. Nat. Neurosci. *24*, 694–704.

Fernández-Ruiz, A., Oliva, A., Soula, M., Rocha-Almeida, F., Nagy, G.A., Martin-Vazquez,

G., and Buzsáki, G. (2021). Gamma rhythm communication between entorhinal cortex and dentate gyrus neuronal assemblies. Science *372*.

Fisahn, A., Pike, F.G., Buhl, E.H., and Paulsen, O. (1998). Cholinergic induction of network oscillations at 40 Hz in the hippocampus in vitro. Nature *394*, 186–189.

Folschweiller, S., and Sauer, J. (2022). Phase-specific pooling of sparse assembly activity by respiration-related brain oscillations. The Journal of Physiology.

Franks, K.M., Russo, M.J., Sosulski, D.L., Mulligan, A.A., Siegelbaum, S.A., and Axel, R. (2011). Recurrent circuitry dynamically shapes the activation of piriform cortex. Neuron *72*, 49–56.

Freeman, W.J. (1960). Correlation of electrical activity of prepyriform cortex and behavior in cat. J. Neurophysiol. *23*, 111–131.

Freeman, W.J., and Skarda, C.A. (1985). Spatial EEG patterns, non-linear dynamics and perception: the neo-Sherringtonian view. Brain Res. *357*, 147–175.

Fries, P., Reynolds, J.H., Rorie, A.E., and Desimone, R. (2001). Modulation of oscillatory neuronal synchronization by selective visual attention. Science *291*, 1560–1563.

Fries, P., Nikolić, D., and Singer, W. (2007). The gamma cycle. Trends Neurosci. *30*, 309–316.

Geweke, J. (1982). Measurement of Linear Dependence and Feedback between Multiple Time Series. Journal of the American Statistical Association *77*, 304–313.

González, J., Cavelli, M., Mondino, A., Rubido, N., Tort, A.B., and Torterolo, P. (2020). Communication Through Coherence by Means of Cross-frequency Coupling. Neuroscience *449*, 157–164.

Gray, C.M., König, P., Engel, A.K., and Singer, W. (1989). Oscillatory responses in cat visual cortex exhibit inter-columnar synchronization which reflects global stimulus properties. Nature *338*, 334–337.

Ito, J., Roy, S., Liu, Y., Cao, Y., Fletcher, M., Lu, L., Boughter, J.D., Grün, S., and Heck, D.H. (2014). Whisker barrel cortex delta oscillations and gamma power in the awake mouse are linked to respiration. Nat. Commun. *5*, 3572.

Lepousez, G., and Lledo, P.-M. (2013). Odor discrimination requires proper olfactory fast oscillations in awake mice. Neuron *80*, 1010–1024.

Li, Q., Takeuchi, Y., Wang, J., Barcsai, L., Pedraza, L.K., Kozák, G., Nakai, S., Kato, S., Kobayashi, K., Ohsawa, M., et al. Reinstating olfactory bulb derived limbic gamma oscillations alleviates depression.

Lisman, J.E., and Jensen, O. (2013). The Theta-Gamma Neural Code. Neuron *77*, 1002–1016.

Lockmann, A.L.V., Laplagne, D.A., Leão, R.N., and Tort, A.B.L. (2016). A Respiration-Coupled Rhythm in the Rat Hippocampus Independent of Theta and Slow Oscillations. J. Neurosci. *36*, 5338–5352.

Lopes-dos-Santos, V., Ribeiro, S., and Tort, A.B.L. (2013). Detecting cell assemblies in large neuronal populations. J. Neurosci. Methods *220*, 149–166.

Lopes-Dos-Santos, V., van de Ven, G.M., Morley, A., Trouche, S., Campo-Urriza, N., and Dupret, D. (2018). Parsing Hippocampal Theta Oscillations by Nested Spectral Components during Spatial Exploration and Memory-Guided Behavior. Neuron *100*, 940–952.e7.

Martin, C., Gervais, R., Messaoudi, B., and Ravel, N. (2006). Learning-induced oscillatory activities correlated to odour recognition: a network activity. Eur. J. Neurosci. *23*, 1801–1810.

Moberly, A.H., Schreck, M., Bhattarai, J.P., Zweifel, L.S., Luo, W., and Ma, M. (2018). Olfactory inputs modulate respiration-related rhythmic activity in the prefrontal cortex and freezing behavior. Nature Communications *9*.

Nagappan, S., and Franks, K.M. (2021). Parallel processing by distinct classes of principal neurons in the olfactory cortex. Elife *10*.

Pashkovski, S.L., Iurilli, G., Brann, D., Chicharro, D., Drummey, K., Franks, K.M., Panzeri, S., and Datta, S.R. (2020). Structure and flexibility in cortical representations of odour space. Nature *583*, 253–258.

Poo, C., and Isaacson, J.S. (2009). Odor Representations in Olfactory Cortex: “Sparse” Coding, Global Inhibition, and Oscillations. Neuron *62*, 850–861.

Rodriguez, E., George, N., Lachaux, J.-P., Martinerie, J., Renault, B., and Varela, F.J. (1999). Perception’s shadow: long-distance synchronization of human brain activity. Nature *397*, 430–433.

Roland, B., Deneux, T., Franks, K.M., Bathellier, B., and Fleischmann, A. (2017). Odor identity coding by distributed ensembles of neurons in the mouse olfactory cortex. Elife *6*.

Scheffer-Teixeira, R., Belchior, H., Caixeta, F.V., Souza, B.C., Ribeiro, S., and Tort, A.B.L. (2012). Theta phase modulates multiple layer-specific oscillations in the CA1 region. Cereb. Cortex *22*, 2404–2414.

Schomburg, E.W., Fernández-Ruiz, A., Mizuseki, K., Berényi, A., Anastassiou, C.A., Koch, C., and Buzsáki, G. (2014). Theta phase segregation of input-specific gamma patterns in entorhinal-hippocampal networks. Neuron *84*, 470–485.

Sirota, A., Montgomery, S., Fujisawa, S., Isomura, Y., Zugaro, M., and Buzsáki, G. (2008). Entrainment of neocortical neurons and gamma oscillations by the hippocampal theta rhythm. Neuron *60*, 683–697.

Tallon-Baudry, C., and Bertrand, O. (1999). Oscillatory gamma activity in humans and its role in object representation. Trends Cogn. Sci. *3*, 151–162.

Tort, A.B.L., Rotstein, H.G., Dugladze, T., Gloveli, T., and Kopell, N.J. (2007). On the formation of gamma-coherent cell assemblies by oriens lacunosum-moleculare interneurons in the hippocampus. Proc. Natl. Acad. Sci. U. S. A. *104*, 13490–13495.

Tort, A.B.L., Kramer, M.A., Thorn, C., Gibson, D.J., Kubota, Y., Graybiel, A.M., and Kopell, N.J. (2008). Dynamic cross-frequency couplings of local field potential oscillations in rat striatum and hippocampus during performance of a T-maze task. Proc. Natl. Acad. Sci. U. S. A. *105*, 20517–20522.

Tort, A.B.L., Komorowski, R.W., Manns, J.R., Kopell, N.J., and Eichenbaum, H. (2009). Theta-gamma coupling increases during the learning of item-context associations. Proc. Natl. Acad. Sci. U. S. A. *106*, 20942–20947.

Tort, A.B.L., Komorowski, R., Eichenbaum, H., and Kopell, N. (2010). Measuring phase-amplitude coupling between neuronal oscillations of different frequencies. J. Neurophysiol. *104*, 1195–1210.

Trouche, S., Perestenko, P.V., van de Ven, G.M., Bratley, C.T., McNamara, C.G., Campo-Urriza, N., Black, S.L., Reijmers, L.G., and Dupret, D. (2016). Recoding a cocaine-place memory engram to a neutral engram in the hippocampus. Nat. Neurosci. *19*, 564–567.

Vanderwolf, C.H. (2000). What is the significance of gamma wave activity in the pyriform cortex? Brain Res. *877*, 125–133.

Wang, X.-J., and Rinzel, J. (1992). Alternating and synchronous rhythms in reciprocally inhibitory model neurons. Neural Comput. *4*, 84–97.

Womelsdorf, T., Fries, P., Mitra, P.P., and Desimone, R. (2006). Gamma-band synchronization in visual cortex predicts speed of change detection. Nature *439*, 733–736.

Yang, Q., Zhou, G., Noto, T., Templer, J.W., Schuele, S.U., Rosenow, J.M., Lane, G., and Zelano, C. (2022). Smell-induced gamma oscillations in human olfactory cortex are required for accurate perception of odor identity. PLoS Biol. *20*, e3001509.

Yanovsky, Y., Ciatipis, M., Draguhn, A., Tort, A.B.L., and Brankačk, J. (2014). Slow oscillations in the mouse hippocampus entrained by nasal respiration. J. Neurosci. *34*, 5949–5964.

Yuval-Greenberg, S., Tomer, O., Keren, A.S., Nelken, I., and Deouell, L.Y. (2008). Transient induced gamma-band response in EEG as a manifestation of miniature saccades. Neuron *58*, 429–441.

Zhong, W., Ciatipis, M., Wolfenstetter, T., Jessberger, J., Müller, C., Ponsel, S., Yanovsky, Y., Brankačk, J., Tort, A.B.L., and Draguhn, A. (2017). Selective entrainment of gamma subbands by different slow network oscillations. Proc. Natl. Acad. Sci. U. S. A. *114*, 4519–4524.

Zibrowski, E.M., and Vanderwolf, C.H. (1997). Oscillatory fast wave activity in the rat pyriform cortex: relations to olfaction and behavior. Brain Res. *766*, 39–49.

Supplementary Material

Mechanisms and functions of respiration-driven gamma oscillations in the piriform cortex

Joaquín González[1*], Pablo Torterolo[1] & Adriano BL Tort[2*]

1 – Departamento de Fisiología, Facultad de Medicina, Universidad de la República, Montevideo, 11200, Uruguay

2 – Brain Institute, Federal University of Rio Grande do Norte, Natal, RN 59056, Brazil

* Correspondence: joaqgonzar@gmail.com or tort@neuro.ufrn.br

Content: 8 Supplementary Figures + Legends
Supplementary Results Section
Supplementary Methods
Supplementary References

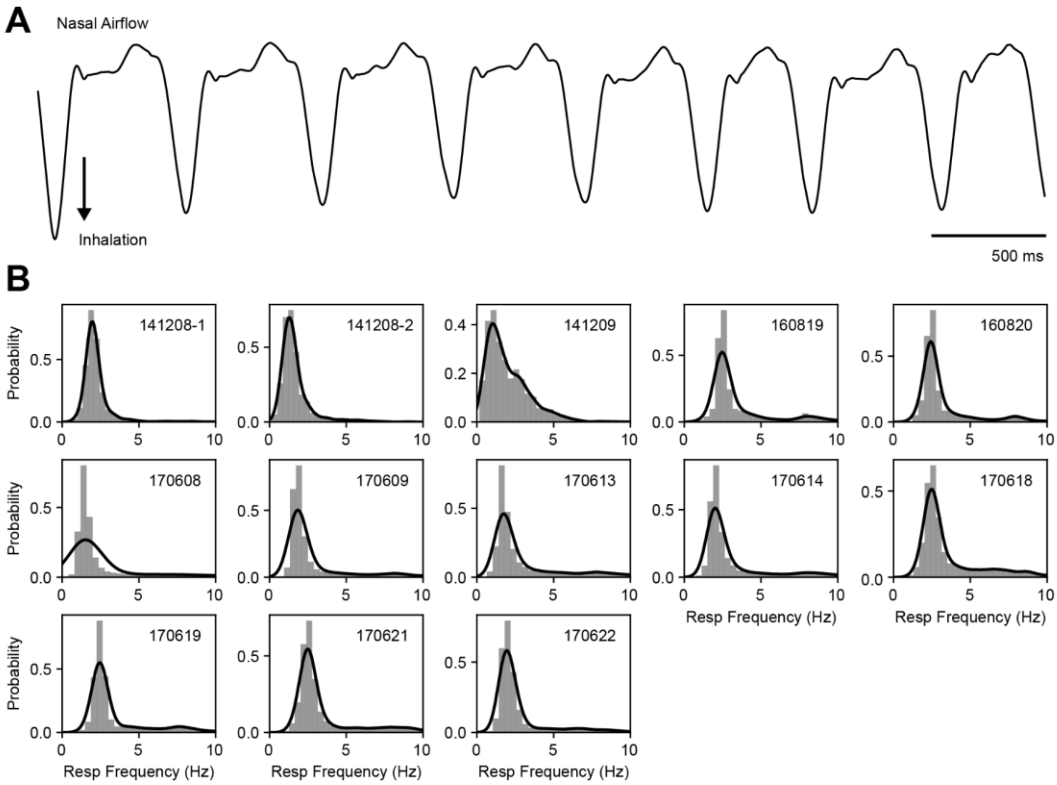

Fig S1. Similar respiratory frequency ranges across mice. A Example of a respiration recording measured through nasal airflow. **B** Respiratory frequency distribution for each mouse (insets show the mouse identification number). The instantaneous breathing frequency was estimated as the inverse of the inhalation period; bars depict probabilities for binned frequency intervals; solid lines show the kde distribution fit.

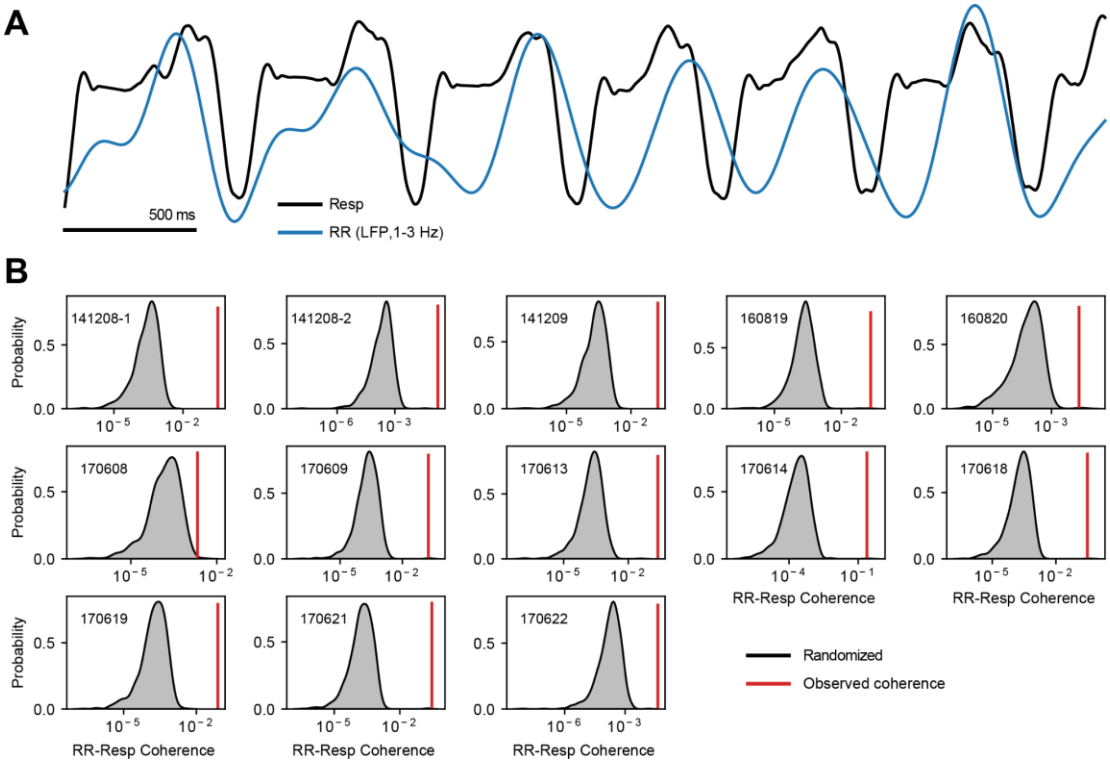

Fig S2. The 1-3 Hz LFP band is entrained by respiration. A Example of a respiration recording (Resp) along with the 1-3 Hz filtered LFP trace, which reflects the respiration-entrained rhythm (RR; see (Tort et al., 2018). **B** Surrogate RR-Resp coherence distributions (insets show the mouse identification number). Each distribution was obtained by computing the RR-Resp coherence using randomly circularly shifted respiration phases (1000 randomizations per mouse). The red vertical lines indicate the actual coherence values. All mice showed significant RR-Resp coherence ($p < 0.01$).

Supplementary Results Section

Respiration-driven low-gamma oscillations fade under anesthesia

After unveiling the mechanisms responsible for the respiration-driven low-gamma activity in the PCx, we investigated whether these oscillations are state-dependent. To that end, we analyzed PCx LFP recordings during ketamine/xylazine anesthesia. Figure S3A shows the LFP spectrogram before and after ketamine/xylazine administration. Anesthesia promoted large-amplitude, slow LFP oscillations while greatly reducing gamma power, an effect that lasted ~30 min (Fig S3A). These results can also be readily seen in the average power spectra of awake vs. anesthetized animals (Fig S3B), thus confirming that PCx low-gamma oscillations depend on the brain state. Next, we investigated if ketamine/xylazine anesthesia alters gamma coupling to respiration by analyzing respiration-LFP phase-amplitude comodulograms. We found that low-gamma oscillations are no longer coupled to respiration during general anesthesia (Fig S3C), despite the respiration-entrained rhythm being still present in the PCx LFP (Fig S3D,E). Intriguingly, the respiration-LFP comodulogram revealed coupling to a faster gamma activity (>80 Hz) under anesthesia (Fig S3C), which we deem likely to relate to the high-frequency oscillations evoked by sub-anesthetic doses of ketamine (Caixeta et al., 2013; Castro-Zaballa et al., 2018; Hunt et al., 2019), though it exhibited no power spectrum peak (c.f. Fig S3B).

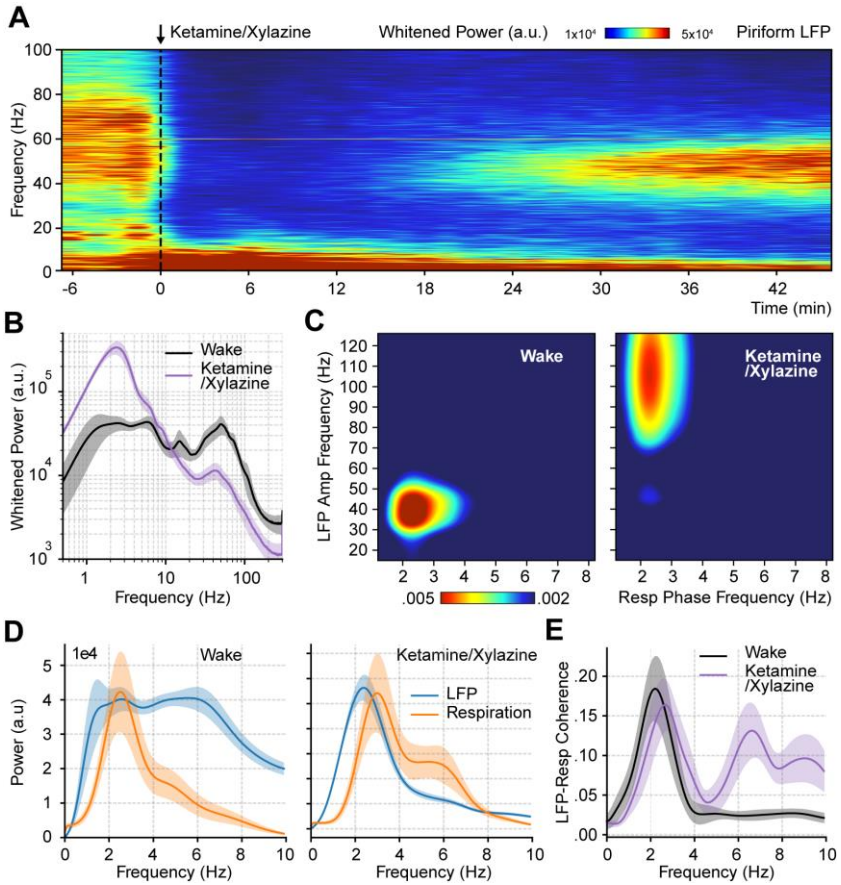

Fig S3. Ketamine/xylazine anesthesia abolishes low-gamma oscillations in the piriform cortex. **A** Spectrogram during ketamine/xylazine anesthesia in a representative animal (time of administration = 0 min). **B** Power spectra for awake and ketamine/xylazine-anesthetized animals (mean ± SEM). **C** Average respiration-LFP comodulogram for either brain state. **D** LFP (blue) and respiration (orange) power spectra (mean ± SEM) during wakefulness (left) and ketamine/xylazine anesthesia (right). **E** LFP-Resp coherence for each state (mean ± SEM).

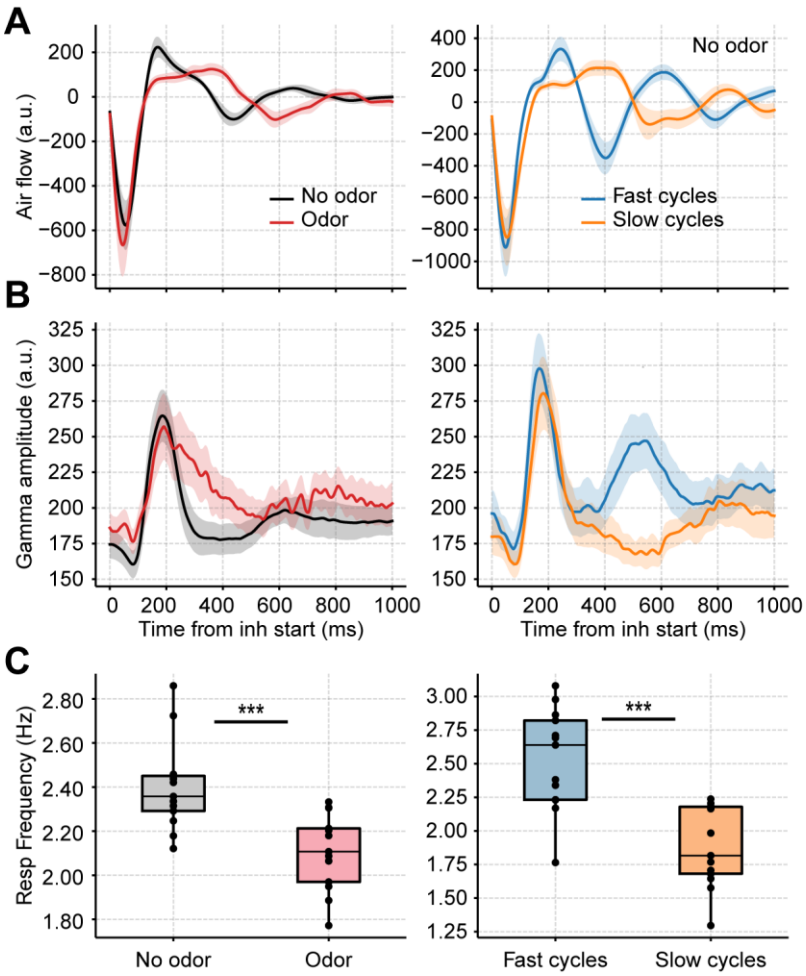

Fig S4. Longer breaths do not account for prolonged gamma activity in response to odors. A Average respiration waveforms triggered by the inhalation start (mean ± SEM). Left: Average breathing cycle in the presence (red) and absence (black) of odors. Right: Average over all fast (blue) and slow (orange) respiratory cycles in the absence of odors. Fast breaths were defined as those with an instantaneous frequency above the 75th percentile; slow breaths as cycles with an instantaneous frequency below the 25th percentile. **B** Average gamma amplitude triggered by inhalation start (mean ± SEM) for the same respiratory cycles as above. **C** Boxplots showing the average respiratory frequency during odor vs no odor cycles (left), and fast vs slow no odor cycles (right). Dots show individual animal values (n = 13 mice).

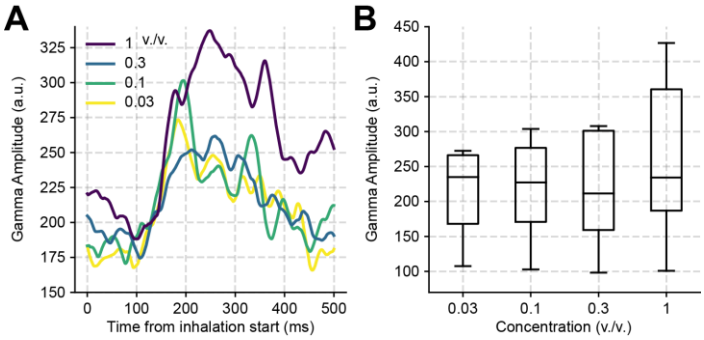

Fig S5. Gamma oscillations change slightly with odor concentration. A Average gamma amplitude triggered by inhalation for ethyl butyrate and hexanal odors delivered at different concentrations (as labeled). Data from both odorants were averaged for these analyses. **B** Left: Boxplots of the mean gamma amplitude for each odor concentration (n = 5 mice).

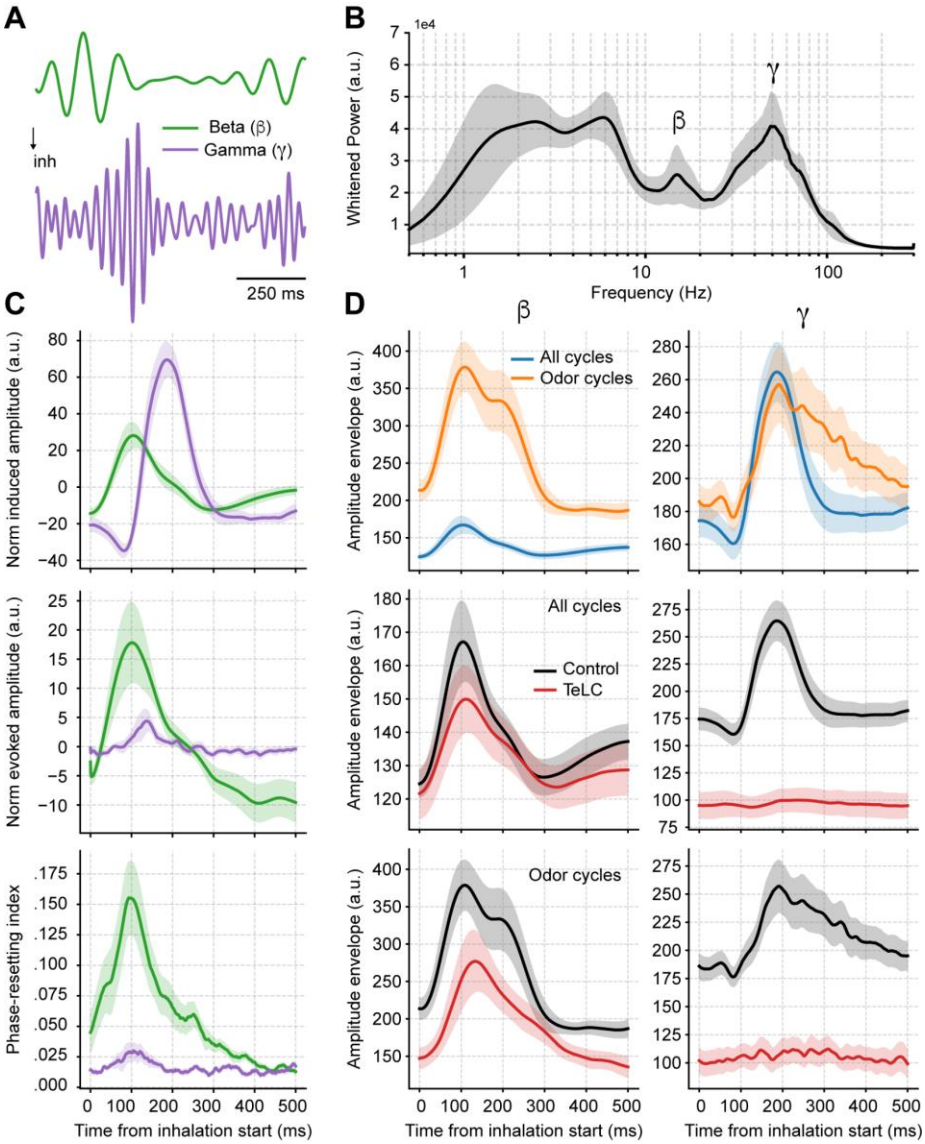

Fig S6. Piriform beta oscillations depend on odor delivery, are evoked at each cycle, and do not require recurrent local computations. A Filtered beta (10-20 Hz) and gamma (30-60 Hz) oscillations**. B** Average LFP power spectrum (± 2*SEM; n = 13 mice). **C** Top: Normalized induced beta (green) and gamma (purple) amplitude triggered by inhalation. Middle: Normalized evoked amplitude. The normalization consisted of removing the average amplitude across time. Bottom: Phase-resetting index for each oscillation. Traces show mean ± SEM. **D** Top: Average beta (left) and gamma (right) amplitude for all respiratory cycles (blue) and only for cycles with odor delivery (orange). We note that because odorless cycles greatly outnumber odor ones (~50-100 to 1), the oscillatory response to all-cycles and the odorless ones is virtually identical (for instance, compare Fig 4A to panel S6D). Middle: Beta and gamma amplitude for all cycles under the control (black) or TeLC (red) condition. Bottom: As above, but for odor cycles. Shades represent the mean ± SEM.

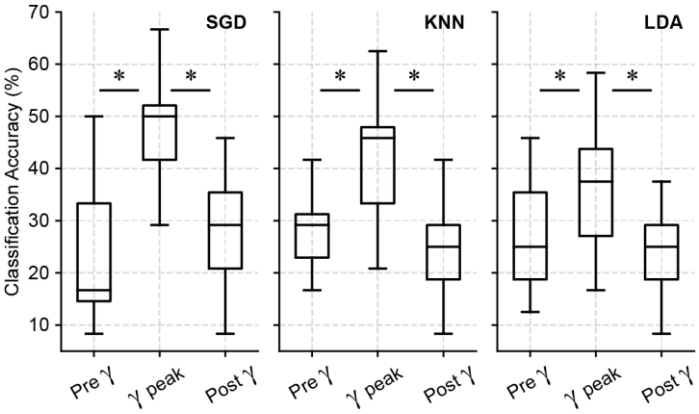

Fig S7. Odor decoding increases during the low-gamma peak. Boxplots showing odor decoding accuracy based on spiking activity measured using 100-ms windows before, during and after the respiration-driven gamma peak (see Methods). Each panel shows results from a different classification model (SGD: stochastic gradient descent classifier; KNN: k-nearest neighbors; LDA: linear discriminant analysis).

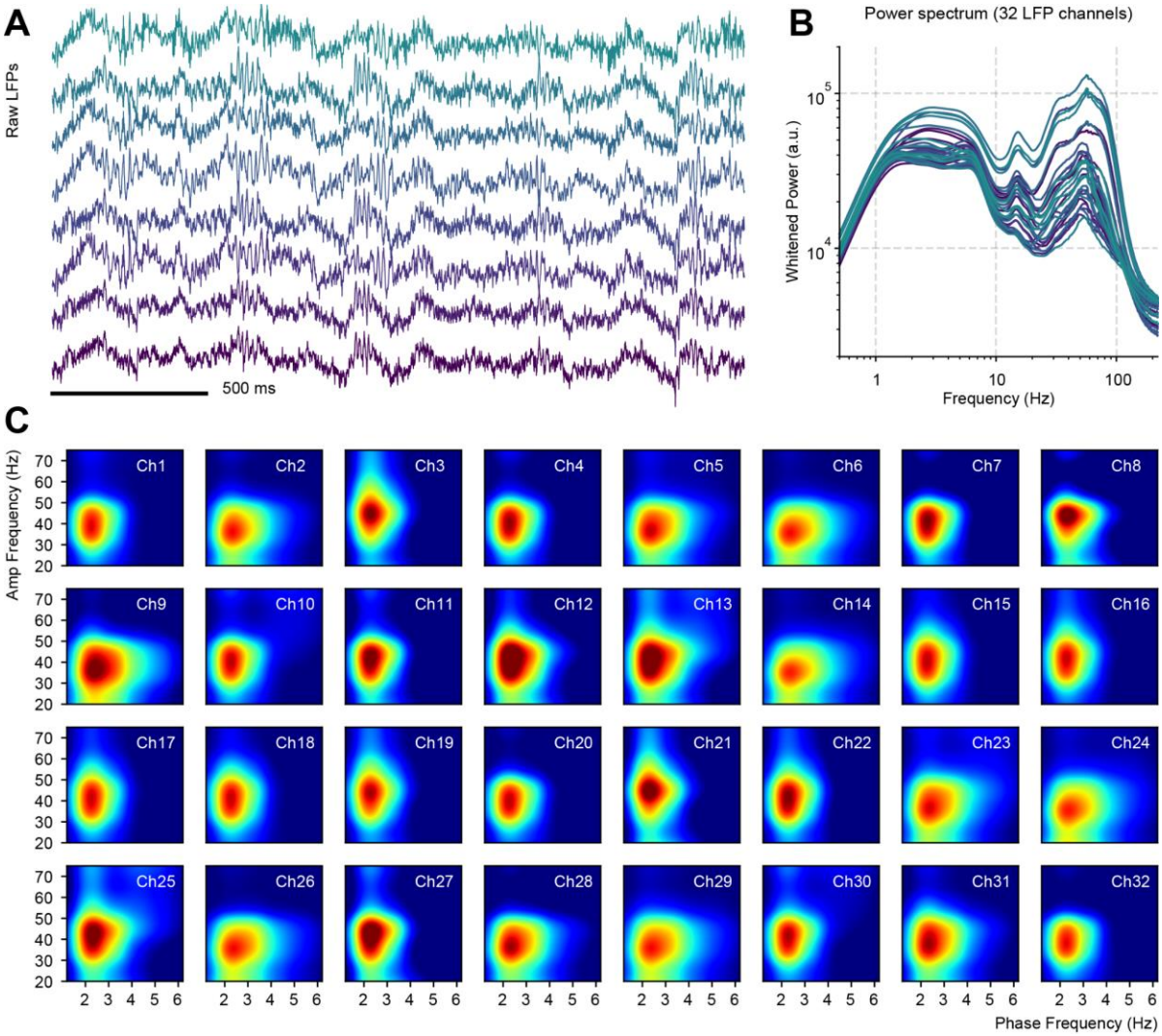

Fig S8. Respiration-driven gamma oscillations in the piriform cortex are evident across recording sites. A Simultaneous LFP recording examples from 8 channels. **B** Whitened LFP power spectra for all 32 recording sites. Colors indicate the electrode number (from green to purple). **C** Phase-amplitude LFP comodulogram for each channel (individual color scales were optimized to depict RR-gamma coupling).

Supplementary Methods

Ketamine/xylazine anesthesia

Ketamine/xylazine (100/10 mg/kg) was administered intraperitoneally in 11/13 mice from the control dataset, inducing stable anesthesia during a 30–45 min time period. A heating pad was used to maintain body temperature during this time. For all analyses, we employed the first 30 minutes following the slow-oscillation onset. A single animal was discarded since no electrophysiological markers of anesthesia were observed.

Induced power, evoked power and phase-resetting index

To study induced power, we (1) filtered the recordings (beta: 10-20 Hz, low-gamma: 30-60 Hz), (2) obtained their amplitude through the Hilbert transform, and (3) computed the inhalation-triggered average. To study evoked power, we (1) filtered the recordings, (2) obtained the inhalation-triggered average, and then (3) estimated the amplitude of the average signal through the Hilbert transform. For obtaining the phase-resetting index of the filtered signals, we used the same procedure as for computing the inter-trial coherence (Makeig et al., 2004) using 500-ms windows following inhalation start as a “trial”.

Supplementary References

Caixeta, F.V., Cornélio, A.M., Scheffer-Teixeira, R., Ribeiro, S., and Tort, A.B.L. (2013). Ketamine alters oscillatory coupling in the hippocampus. Sci. Rep. *3*, 2348.

Castro-Zaballa, S., Cavelli, M.L., Gonzalez, J., Nardi, A.E., Machado, S., Scorza, C., and Torterolo, P. (2018). EEG 40 Hz Coherence Decreases in REM Sleep and Ketamine Model of Psychosis. Front. Psychiatry *9*, 766.

Hunt, M.J., Adams, N.E., Średniawa, W., Wójcik, D.K., Simon, A., Kasicki, S., and Whittington, M.A. (2019). The olfactory bulb is a source of high-frequency oscillations (130-180 Hz) associated with a subanesthetic dose of ketamine in rodents. Neuropsychopharmacology *44*, 435–442.

Makeig, S., Debener, S., Onton, J., and Delorme, A. (2004). Mining event-related brain dynamics. Trends Cogn. Sci. *8*, 204–210.

Tort, A.B.L., Brankačk, J., and Draguhn, A. (2018). Respiration-Entrained Brain Rhythms Are Global but Often Overlooked. Trends Neurosci. *41*, 186–197.